

Horizontal expansion of biicosahedral  $M_{13}$ -based nanoclusters: resolving decades-long questions†Cite this: *Nanoscale Horiz.*, 2022, 7, 1397Received 8th July 2022,  
Accepted 23rd September 2022

DOI: 10.1039/d2nh00321j

rsc.li/nanoscale-horizons

Chuanjun Zhou,<sup>‡,ab</sup> Peiyao Pan,<sup>‡,ab</sup> Xiao Wei,<sup>ab</sup> Zidong Lin,<sup>c</sup> Cheng Chen,<sup>c</sup>  
Xi Kang <sup>\*ab</sup> and Manzhou Zhu <sup>\*ab</sup>

For metal nanoclusters with the “cluster of clusters” intramolecular evolution pattern, most efforts have been made towards the vertical superposition of icosahedral nanobuilding blocks (e.g., from mono-icosahedral  $Au_{13}$  to bi-icosahedral  $Au_{25}$  and tri-icosahedral  $Au_{37}$ ), while the horizontal expansion of these rod-shaped multi-icosahedral aggregates was largely neglected. We herein report the horizontal expansion of the biicosahedral  $M_{25}$  cluster framework, yielding an  $[Au_{19}Ag_{12}(S-Adm)_6(DPPM)_6Cl_7]^{2+}$  nanocluster that contains an  $Au_{13}Ag_{12}$  kernel and six  $Au_1(DPPM)_1(S-Adm)_1$  peripheral wings. The structural determination of  $[Au_{19}Ag_{12}(S-Adm)_6(DPPM)_6Cl_7]^{2+}$  resolved a decades-long question towards rod-shaped multi-icosahedral aggregates: how to load bidentate phosphine and bulky thiol ligands onto the nanocluster framework? The structural comparison between  $[Au_{19}Ag_{12}(S-Adm)_6(DPPM)_6Cl_7]^{2+}$  and previously reported  $[Au_{13}Ag_{12}(PPh_3)_{10}Cl_8]^{2+}$  or  $[Au_{13}Ag_{12}(SR)_5(PPh_3)_{10}Cl_2]^{2+}$  rationalized the unique packing of  $Au_1(DPPM)_1(S-Adm)_1$  motif structures on the surface of the former nanocluster. Overall, this work presents the horizontal expansion of rod-shaped multi-icosahedral nanoclusters, which provides new insights into the preparation of novel icosahedron-based aggregates with both vertically and horizontally growing extensions.

## 1. Introduction

Metal nanoclusters have served as an emerging class of modular nanomaterials owing to their atomically precise structures

## New concepts

The “cluster of clusters” evolution was one of the most fascinating features of intramolecular assembled nanoclusters. Hundreds of clusters have been constructed by systematically aggregating icosahedral  $M_{13}$  nanobuilding blocks, and these rod-shaped aggregates were extensively studied owing to the strong electron coupling between substituent icosahedral units. However, most efforts were made towards the vertical superposition of icosahedral nanobuilding blocks (e.g., from mono-icosahedral  $Au_{13}$  to bi-icosahedral  $Au_{25}$  and tri-icosahedral  $Au_{37}$ ), while the horizontal expansion of these rod-shaped multi-icosahedral aggregates was largely neglected. In this work, based on a newly developed  $M_{31}$  nanocluster template, the horizontal expansion of the biicosahedral  $M_{25}$  dimer has been accomplished. The atomic-level structural determination of the  $Au_{19}Ag_{12}(S-Adm)_6(DPPM)_6Cl_7$  cluster resolved two decades-long questions for rod-shaped multi-icosahedral aggregates, including (i) how to load bidentate phosphine ligands onto the nanocluster shoulder and (ii) how to arrange bulky thiol ligands onto the nanocluster waist. This work significantly broadens the research towards the “cluster of clusters” evolution pattern of metal nanoclusters.

and intriguing physical–chemical properties.<sup>1–8</sup> Besides, due to their programmable structure-dependent performances, metal nanoclusters or cluster-based hybrids have been customized for widespread applications such as catalysis, chemical sensors, drug delivery, biological imaging, and so on.<sup>9–18</sup> Typically, the structure of nanoclusters is composed of an internal metallic kernel and a peripheral ligand shell.<sup>19–30</sup> The structural determination of the metallic kernels of clusters at the atomic level has considerably inspired nanoscientists on a long-lasting question in nanoscience: what are the evolution modes from small-sized metallic complexes to nanoclusters or from nanoclusters to large-sized nanoparticles?<sup>1,31</sup> Indeed, such a question has puzzled nanoscientists for decades because of two objective deficiencies of metal nanoparticles: the nonuniform molecule size and the uncertain surface environment.

With the continuous accumulation of the determined structures of metal nanoclusters, several intracluster evolution patterns have been observed experimentally, including cluster of

<sup>a</sup> Department of Chemistry and Centre for Atomic Engineering of Advanced Materials, Anhui Province Key Laboratory of Chemistry for Inorganic/Organic Hybrid Functionalized Materials, Anhui University, Hefei 230601, P. R. China. E-mail: kangxi\_chem@ahu.edu.cn, zmz@ahu.edu.cn

<sup>b</sup> Key Laboratory of Structure and Functional Regulation of Hybrid Materials, Ministry of Education, Anhui University, Hefei 230601, P. R. China

<sup>c</sup> Institutes of Physical Science and Information Technology, Anhui University, Hefei, Anhui 230601, P. R. China

† Electronic supplementary information (ESI) available. CCDC 2183917, 2163571, 2163572 and 2163804. For ESI and crystallographic data in CIF or other electronic format see DOI: <https://doi.org/10.1039/d2nh00321j>

‡ These authors contributed equally to this work.

clusters, kernel fusion, interpenetration, shell-by-shell, layer-by-layer, tetrahedron-based vertex-sharing, *etc.*<sup>31</sup> Among these patterns, the “cluster of clusters”, which is first proposed in the 1980s, represents one of the most fascinating features of intramolecular assembled nanoclusters.<sup>32–35</sup> The icosahedral  $M_{13}$  nanobuilding blocks can be aggregated by a vertex-sharing mode (*e.g.*, rod-shaped  $Au_{25}$ ,  $Pt_2Ag_{23}$ ,  $Au_{37}$ ,  $Pt_3Ag_{44}$ , and  $Ag_{61}$ ,<sup>36–40</sup> and pan-shaped  $Au_{34}Cu_3$ ,  $Pt_3Ag_{33}$ , and  $Au_{60}$ ),<sup>41–43</sup> a face-sharing mode (*e.g.*,  $Au_{38}$  and  $Au_{27}Cd_1$ ),<sup>44,45</sup> or an interpenetrating mode (*e.g.*,  $Au_8Ag_{55}$ ,  $Au_8Ag_{57}$ , and  $Au_{156}$ ).<sup>46,47</sup>

Among the cluster of clusters, rod-shaped aggregates of  $M_{13}$  ( $M = Au/Ag/Cu/Pt/Pd/Ni$ ) nanobuilding blocks have been extensively studied because of the strong electron coupling between substituent icosahedral units.<sup>31–35,40</sup> However, most efforts were made towards the vertical superposition of icosahedral units (*e.g.*, from mono-icosahedral  $Au_{13}$  to bi-icosahedral  $Au_{25}$  and tri-icosahedral  $Au_{37}$ ), while the horizontal expansion of these rod-shaped multi-icosahedral aggregates is largely neglected.<sup>31</sup> Besides, several questions remain unsolved regarding these nanoclusters. For example, for rod-shaped  $Au_{25}(PPh_3)_{10}(SR)_5Cl_2$  with five monodentate  $PPh_3$  at each shoulder and five thiol ligands at the waist,<sup>36</sup> the outcome remains mysterious by substituting the monodentate  $PPh_3$  with bidentate phosphine ligands or regulating the SR as bulky thiol ligands in terms of two objective contradictions: (i) the odd-numbered coordination sites at the nanocluster shoulder (*i.e.*, 5) *versus* the even-numbered coordination ability (*i.e.*,  $2n$ ) of the bidentate phosphines, and (ii) the limited space at the nanocluster waist *versus* the large steric hindrance of bulky thiols. The problem solving towards such rod-shaped cluster models calls for more efforts.

Herein, the horizontal expansion of the rod-shaped biicosahedral  $M_{25}$  nanocluster was accomplished, yielding an  $[Au_{19}Ag_{12}(S-Adm)_6(DPPM)_6Cl_7]^{2+}$  nanocluster ( $Au_{19}Ag_{12}$  for short; S-Adm = 1-adamantanethiol; DPPM = bis(diphenylphosphino)methane) that consists of a biicosahedral  $Au_{13}Ag_{12}$  kernel, seven chlorine ligands, and six  $Au_1(DPPM)_1(S-Adm)_1$  peripheral wings. Compared with the rod-shaped  $[Au_{13}Ag_{12}(SR)_5(PPh_3)_{10}Cl_2]^{2+}$  or  $[Au_{13}Ag_{12}(PPh_3)_{10}Cl_8]^{2+}$  ( $Au_{13}Ag_{12}-S$  or  $Au_{13}Ag_{12}-Cl$  for short), the horizontal extension of unique  $Au_1(DPPM)_1(S-Adm)_1$  surface units in  $Au_{19}Ag_{12}$  was rationalized by the substitution of monodentate  $PPh_3$  with bidentate DPPM as well as the introduction of bulky S-Adm ligands. Control experiments were carried out to validate the decisive roles of both bidentate DPPM and bulky S-Adm in constructing the  $Au_{19}Ag_{12}$  nanocluster. In this context,  $Au_{19}Ag_{12}$  has served as a cluster model for resolving the above-mentioned longstanding questions in rod-shaped nanoclusters with the “cluster of clusters” intramolecular evolution pattern.

## 2. Results and discussion

The rod-shaped  $Au_{13}Ag_{12}-S$  nanocluster follows a biicosahedral configuration *via* sharing a vertex Au atom between two  $Au_7Ag_6$  nanobuilding blocks.<sup>48</sup> The Au atoms at the nanocluster shoulder are capped by monodentate  $PPh_3$  ligands, and the

Ag atoms at the nanocluster waist are stabilized by  $SC_2H_4Ph$  ligands. Two longstanding questions remain unsolved for this nanocluster template (Scheme 1).

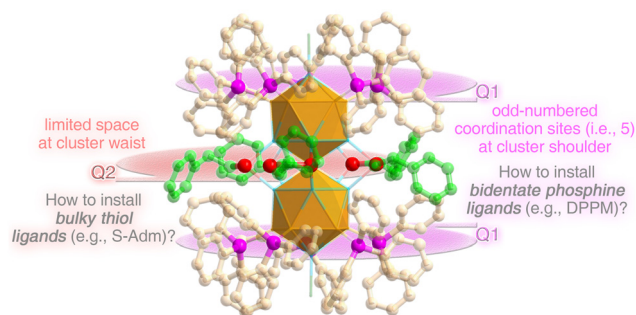
(i) Altering monodentate  $PPh_3$  into bidentate phosphine ligands at the nanocluster shoulder (Scheme 1, Q1): five  $PPh_3$  ligands are anchored onto each cluster shoulder *via* Au–P interactions, which puts forward a contradiction between the odd-numbered coordination sites (*i.e.*, 5) and the even-numbered coordination ability (*i.e.*,  $2n$ ) of the bidentate phosphines (*e.g.*, DPPM).

(ii) Arranging bulky thiol ligands into the limited space at the nanocluster waist (Scheme 1, Q2): five  $-SC_2H_4Ph$  ligands are arranged at the waist of  $Au_{13}Ag_{12}-S$  *via* Ag–S–Ag interactions. The waist space of the nanocluster is limited by considering the steric hindrance of the  $M_{25}$  metallic kernel from the inside out as well as the hindrance of the phosphine ligands from both sides to the middle. Accordingly, the thiol ligands in reported biicosahedral  $M_{25}$  nanoclusters are almost accompanied by alkyl chains or benzene rings with relatively small steric resistances. However, it remains challenging to install bulky thiol ligands (*e.g.*, S-Adm) into this limited space.

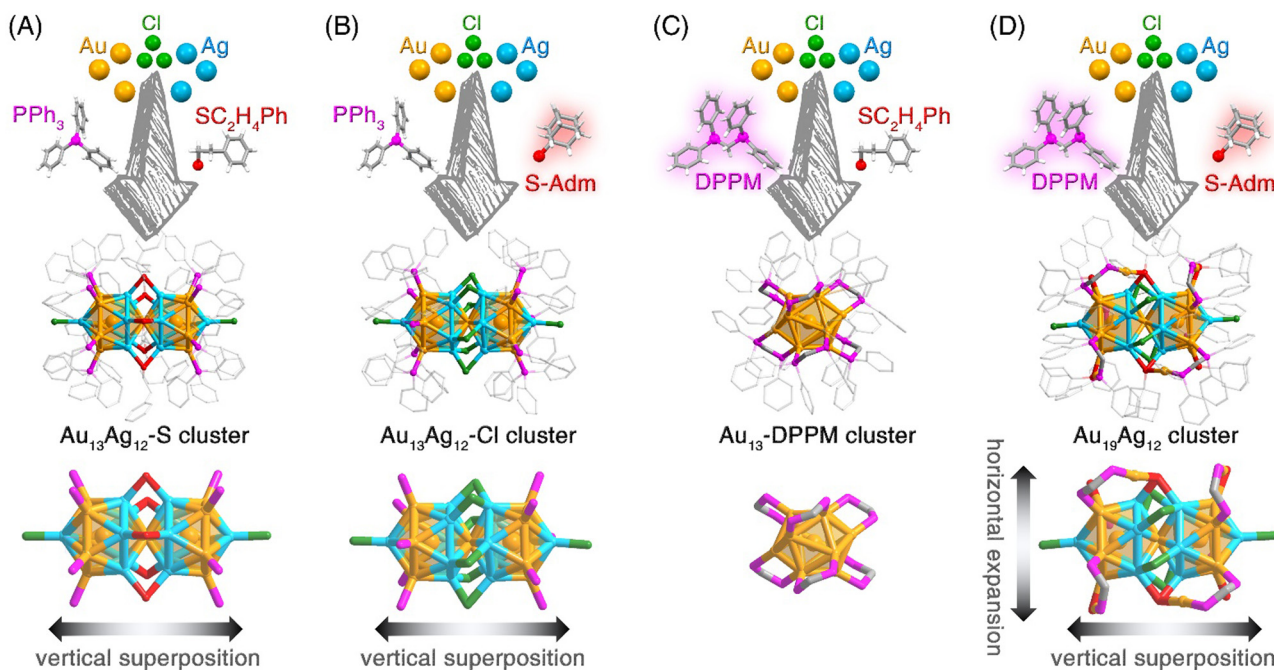
Collectively, it is unclear how the nanocluster framework undergoes self-adaptation in the presence of bidentate phosphine ligands or bulky thiol ligands, and a comprehensive understanding of these longstanding questions calls for a new nanocluster template established from the biicosahedral  $M_{25}$  nanostructure.

Several efforts have been made to install bidentate DPPM or bulky S-Adm ligands onto the  $M_{25}$  nanocluster surface (Scheme 2). The rod-shaped  $Au_{13}Ag_{12}-S$  nanocluster was synthesized by directly reducing the Au–Ag–Cl– $PPh_3$ – $SC_2H_4Ph$  complexes with  $NaBH_4$  (Scheme 2A). A set of control experiments were performed (Scheme 2B–D).

(i) The single thiol ligand control (Scheme 2B): the  $SC_2H_4Ph$  was substituted by the bulky S-Adm ligand, while the other experimental conditions remained unchanged. The  $Au_{13}Ag_{12}-Cl$



**Scheme 1** Schematic illustration of two long-lasting questions towards the rod-like biicosahedral  $M_{25}$  cluster template. (Q1) The substitution of monodentate  $PPh_3$  with bidentate phosphine ligands at the nanocluster shoulder. (Q2) The arrangement of bulky thiol ligands into the limited space at the nanocluster waist. The  $[Au_{13}Ag_{12}(SC_2H_4Ph)_5(PPh_3)_{10}Cl_2]^{2+}$  nanocluster was exploited as the nanocluster model. Color labels: orange sphere, Au; light blue sphere, Ag; green sphere, Cl; red sphere, S; magenta sphere, P; pale pink sphere, C on  $PPh_3$  ligands; pale green sphere, C on  $SC_2H_4Ph$  ligands. For clarity, all H atoms are omitted.



**Scheme 2** Efforts for installing bidentate DPPM and bulky S-Adm ligands onto the biicosahedral nanocluster surface. (A) The preparation of the  $\text{Au}_{13}\text{Ag}_{12}\text{-S}$  nanocluster. (B) The preparation of the  $\text{Au}_{13}\text{Ag}_{12}\text{-Cl}$  nanocluster. (C) The preparation of the  $\text{Au}_{13}\text{-DPPM}$  nanocluster. (D) The preparation of the  $\text{Au}_{19}\text{Ag}_{12}$  nanocluster. Color labels: orange sphere, Au; light blue sphere, Ag; green sphere, Cl; red sphere, S; magenta sphere, P; grey sphere, C; white sphere, H.

nanocluster was obtained without surface thiol ligands.<sup>49</sup> The  $\text{Au}_{13}\text{Ag}_{12}\text{-Cl}$  nanocluster followed a similar configuration to  $\text{Au}_{13}\text{Ag}_{12}\text{-S}$  with the only difference of waist stabilizers. For  $\text{Au}_{13}\text{Ag}_{12}\text{-Cl}$ , six chlorine ligands stabilized the biicosahedral configuration *via* Ag–Cl–Ag interactions, playing the same role as  $\text{SC}_2\text{H}_4\text{Ph}$  ligands in  $\text{Au}_{13}\text{Ag}_{12}\text{-S}$ . In other words, compared with  $\text{SC}_2\text{H}_4\text{Ph}$ , the bulky thiol ligand was challenging to be installed at the nanocluster waist, which was probably due to the large steric hindrance of S-Adm relative to the limited space.

(ii) The single phosphine ligand control (Scheme 2C): the substitution of  $\text{PPh}_3$  with DPPM yielded a homogold  $[\text{Au}_{13}(\text{DPPM})_6]^{3+}$  ( $\text{Au}_{13}\text{-DPPM}$  for short) nanocluster. Accordingly, the biicosahedral configuration of  $\text{M}_{25}$  was broken to give rise to a mono-icosahedral nanocluster. The twelve surface Au atoms of the  $\text{Au}_{13}\text{-DPPM}$  nanocluster were capped by six DPPM ligands with an Au–DPPM–Au bonding mode. The obtained  $\text{Au}_{13}\text{-DPPM}$  nanocluster was the same as the previously reported one that was prepared *via* a thiol addition-induced synthetic procedure.<sup>50</sup> Of note, the Ag component was absent in the final  $\text{Au}_{13}\text{-DPPM}$ . Such an absence might result from the instability of the possible  $\text{Ag}_x\text{Au}_{13-x}(\text{DPPM})_6$  products that only the homogold  $\text{Au}_{13}\text{-DPPM}$  nanocluster survived.

(iii) The dual thiol and phosphine ligand control (Scheme 2D): the  $\text{PPh}_3$  and  $\text{SC}_2\text{H}_4\text{Ph}$  were substituted by bidentate DPPM and bulky S-Adm ligands simultaneously, which produced an  $\text{Au}_{19}\text{Ag}_{12}$  nanocluster. The  $\text{Au}_{19}\text{Ag}_{12}$  contained an  $\text{M}_{25}$  biicosahedron that was co-stabilized by Cl, DPPM, and S-Adm ligands. The rod-shaped  $\text{M}_{25}$  kernel was maintained by

comparing the overall structure of  $\text{Au}_{19}\text{Ag}_{12}$  to that of  $\text{Au}_{13}\text{Ag}_{12}\text{-S}$  or  $\text{Au}_{13}\text{Ag}_{12}\text{-Cl}$ , while the surface DPPM–Au–S-Adm motif structures followed a horizontal expansion mode. Collectively, based on the horizontally expanded biicosahedral  $\text{Au}_{19}\text{Ag}_{12}$  nanocluster, both bidentate phosphine and bulky thiol ligands were installed onto the surface of rod-shaped nanoclusters.

The ESI-MS results of the  $\text{Au}_{19}\text{Ag}_{12}$  nanocluster showed two groups of mass signals around 2853 and 4297 Da, corresponding to  $[\text{Au}_{31-x}\text{Ag}_x(\text{S-Adm})_6(\text{DPPM})_6\text{Cl}_7]^{3+}$  and  $[\text{Au}_{31-x}\text{Ag}_x(\text{S-Adm})_6(\text{DPPM})_6\text{Cl}_7]^{2+}$  ( $x = 10\text{--}14$ ), respectively (Fig. S1, ESI<sup>†</sup>). The excellent agreement of the experimental and simulated isotope patterns illustrated that the measured formulas of the largest peaks within these two groups were  $[\text{Au}_{19}\text{Ag}_{12}(\text{S-Adm})_6(\text{DPPM})_6\text{Cl}_7]^{3+}$  and  $[\text{Au}_{19}\text{Ag}_{12}(\text{S-Adm})_6(\text{DPPM})_6\text{Cl}_7]^{2+}$  (Fig. S1, insets, ESI<sup>†</sup>). In addition, ESI-MS results demonstrated that several metal positions of the  $\text{Au}_{19}\text{Ag}_{12}$  nanocluster framework were jointly occupied by Au/Ag, which was reminiscent of the composition of  $\text{Au}_{13}\text{Ag}_{12}\text{-S}$ .<sup>48</sup> By combining the ESI-MS results and the crystal data, such  $\text{Au}_{31-x}\text{Ag}_x(\text{S-Adm})_6(\text{DPPM})_6\text{Cl}_7$  nanoclusters are called  $\text{Au}_{19}\text{Ag}_{12}$  in this work (see Tables S5–S7, ESI<sup>†</sup> for more details of the naming of the three alloy nanoclusters in this work). Besides, previous studies of  $\text{M}_{13}$ -based cluster aggregates demonstrated that each icosahedral unit tended to hold eight free valence electrons within the nanocluster framework.<sup>31</sup> Accordingly, for the  $[\text{Au}_{19}\text{Ag}_{12}(\text{S-Adm})_6(\text{DPPM})_6\text{Cl}_7]^{2+}$  mass signal, the nominal electron count of the  $\text{Au}_{19}\text{Ag}_{12}$  nanocluster was determined as 16 (*i.e.*,  $31(\text{Au} + \text{Ag}) - 6(\text{S-Adm}) - 7(\text{Cl}) - 2(\text{charge}) = 16e$ ),<sup>51</sup> tallying with the two icosahedral units in the cluster framework. The presence of

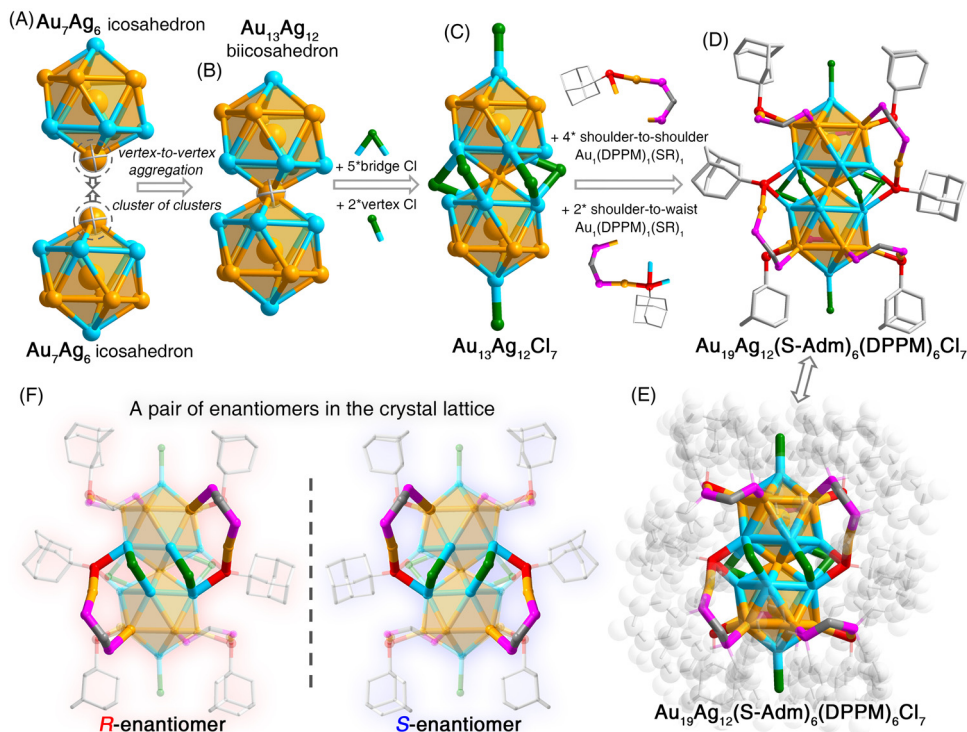


**Fig. 1** Structural anatomy of the  $\text{Au}_{19}\text{Ag}_{12}$  nanocluster. (A) The mono-icosahedral  $\text{Au}_7\text{Ag}_6$  unit. (B) The biicosahedral  $\text{Au}_{13}\text{Ag}_{12}$  kernel. (C) The  $\text{Au}_{13}\text{Ag}_{12}\text{Cl}_7$  structure with two vertex Cl and five waist Cl ligands. (D) The  $\text{Au}_{19}\text{Ag}_{12}(\text{S-Adm})_6(\text{DPPM})_6\text{Cl}_7$  with four shoulder-to-shoulder  $\text{Au}_1(\text{DPPM})_1(\text{SR})_1$  and two shoulder-to-waist  $\text{Au}_1(\text{DPPM})_1(\text{SR})_1$  surface motif structures. For clarity, the benzene rings on DPPM are omitted. (E) The overall structure of  $\text{Au}_{19}\text{Ag}_{12}(\text{S-Adm})_6(\text{DPPM})_6\text{Cl}_7$ . (F) A pair of nanocluster enantiomers in the crystal lattice. Color labels: orange sphere, Au; light blue sphere, Ag; green sphere, Cl; red sphere, S; magenta sphere, P; grey sphere, C; white sphere, H.

$[\text{Au}_{31-x}\text{Ag}_x(\text{S-Adm})_6(\text{DPPM})_6\text{Cl}_7]^{3+}$  signals originated from the loss of an electron from the nanocluster molecule, which has also been observed previously in  $\text{Ag}_{44}(\text{SR})_{30}$  and  $\text{Pt}_1\text{Ag}_{31}(\text{SR})_{16}(\text{DPPM})_3\text{Cl}_3$  nanoclusters.<sup>52,53</sup>

The structural anatomy of the  $\text{Au}_{19}\text{Ag}_{12}$  nanocluster is shown in Fig. 1 and Fig. S2 (ESI<sup>†</sup>). First, two  $\text{Au}_7\text{Ag}_6$  icosahedral nanobuilding blocks were assembled *via* sharing the vertex Au atom, giving rise to an  $\text{Au}_{13}\text{Ag}_{12}$  biicosahedral kernel (Fig. 1A and B). Then, seven chlorine ligands, including five bridge Cl ligands at the waist and two Cl ligands at the vertex, were bonded onto the  $\text{Au}_{13}\text{Ag}_{12}$  biicosahedron to yield an  $\text{Au}_{13}\text{Ag}_{12}\text{Cl}_7$  structure (Fig. 1C). Finally, the  $\text{Au}_{13}\text{Ag}_{12}\text{Cl}_7$  structure was enwrapped by six  $\text{Au}_1(\text{DPPM})_1(\text{S-Adm})_1$  surface motif units to generate the overall structure of  $\text{Au}_{19}\text{Ag}_{12}$  (Fig. 1D and E). Among these DPPM–Au–SAdm surface motifs, four were anchored onto the nanocluster with a shoulder-to-shoulder pattern, while the other two followed a shoulder to waist pattern. As shown in Fig. 1D and E, all bidentate DPPM ligands dually bound with a shoulder Au atom and a motif Au atom, while the bulky S-Adm ligands connected a shoulder Au atom and a motif Au atom (for motifs with a shoulder-to-shoulder pattern) or two waist Ag atoms and a motif Au atom (for motifs with a shoulder-to-waist pattern).

Two nanocluster enantiomers of the  $\text{Au}_{19}\text{Ag}_{12}$  nanocluster were observed in the crystal lattice (Fig. 1F and Fig. S3, ESI<sup>†</sup>). Fig. 1F shows the mirrored structures of *R*-nanocluster and

*S*-nanocluster enantiomers. Furthermore, the crystallographic packing of these enantiomers followed a “lamellar eutectic” pattern, and the interlayer distance was determined as 28.897 Å from the (100) plane (Fig. S3, ESI<sup>†</sup>). Such a crystallographic packing pattern has been observed in several other crystal lattices consisting of nanocluster enantiomers.<sup>54,55</sup>

Structurally, both  $\text{Au}_{13}\text{Ag}_{12}\text{-S}$  and  $\text{Au}_{13}\text{Ag}_{12}\text{-Cl}$  nanoclusters follow a “cluster of clusters” evolution mode and are assembled through the vertical superposition of icosahedral nanobuilding blocks. By comparison, the  $\text{Au}_{19}\text{Ag}_{12}$  nanocluster is constructed by horizontally expanding the rod-like biicosahedral  $\text{M}_{25}$  cluster framework with several denotative  $\text{Au}_1(\text{DPPM})_1(\text{S-Adm})_1$  motif structures (Fig. 2). A combination of  $\text{Au}_{13}\text{Ag}_{12}\text{-S}$ ,  $\text{Au}_{13}\text{Ag}_{12}\text{-Cl}$ , and  $\text{Au}_{19}\text{Ag}_{12}$  nanoclusters forms a platform for investigating the ligand effect in vertically and horizontally extending the  $\text{M}_{25}$  framework (Fig. 2). It is suggested that the biicosahedral  $\text{M}_{25}$  framework is robust enough to load five thiol ligands or six chlorine ligands into the limited space at the nanocluster waist, yielding the  $\text{Au}_{13}\text{Ag}_{12}\text{-S}$  or  $\text{Au}_{13}\text{Ag}_{12}\text{-Cl}$ , respectively. Besides, although the bulky S-Adm ligands cannot be included into the limited space of the  $\text{M}_{25}$  framework, the further introduction of DPPM ligands triggers the self-adaption of the  $\text{M}_{25}$  framework. As a result, six couples of DPPM and S-Adm ligands are anchored onto the framework surface by tying six Au atoms. For the assembly between two  $\text{M}_{13}$  icosahedra, because of the pulling effect of surface  $\text{Au}_1(\text{DPPM})_1$

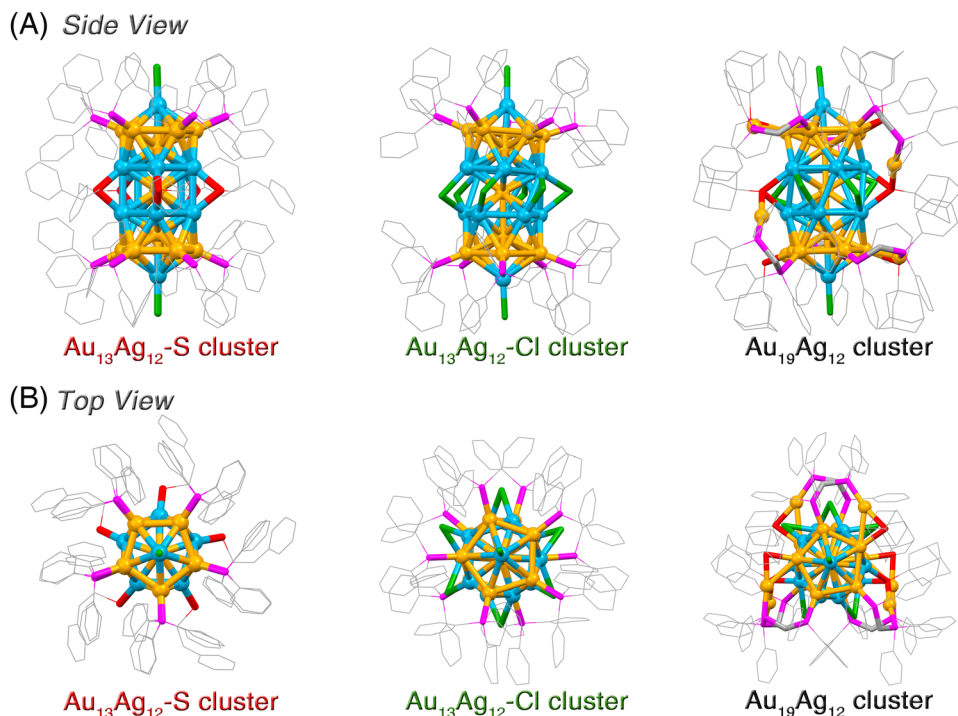


Fig. 2 Structural comparison among  $\text{Au}_{13}\text{Ag}_{12}\text{-S}$ ,  $\text{Au}_{13}\text{Ag}_{12}\text{-Cl}$ , and  $\text{Au}_{19}\text{Ag}_{12}$  nanoclusters with a similar biicosahedral  $\text{Au}_{13}\text{Ag}_{12}$  kernel. (A) Side views of  $\text{Au}_{13}\text{Ag}_{12}\text{-S}$ ,  $\text{Au}_{13}\text{Ag}_{12}\text{-Cl}$ , and  $\text{Au}_{19}\text{Ag}_{12}$  nanoclusters. (B) Top views of  $\text{Au}_{13}\text{Ag}_{12}\text{-S}$ ,  $\text{Au}_{13}\text{Ag}_{12}\text{-Cl}$ , and  $\text{Au}_{19}\text{Ag}_{12}$  nanoclusters. Color labels: orange sphere, Au; light blue sphere, Ag; green sphere, Cl; red sphere, S; magenta sphere, P; grey sphere, C. For clarity, all H atoms are omitted.

(S-Adm)<sub>1</sub> motif structures, the distortion degree of icosahedral  $\text{Au}_7\text{Ag}_6$  nanobuilding blocks in  $\text{Au}_{19}\text{Ag}_{12}$  is higher than that in  $\text{Au}_{13}\text{Ag}_{12}\text{-S}$  or  $\text{Au}_{13}\text{Ag}_{12}\text{-Cl}$ .

The comparison of the corresponding bond lengths is depicted in Fig. S4 (ESI<sup>†</sup>). Specifically, the bond length distributions of these  $\text{M}_{13}$ -assembled nanoclusters (*i.e.*,  $\text{Au}_{13}\text{Ag}_{12}\text{-S}$ ,  $\text{Au}_{13}\text{Ag}_{12}\text{-Cl}$ , and  $\text{Au}_{19}\text{Ag}_{12}$ ) are similar in terms of the Au(kernel)–M(icosahedral surface), M(icosahedral surface)–M(icosahedral surface), Ag(icosahedral surface)–Cl(vertex), and Au(icosahedral surface)–P(shoulder) bonds (M = Au/Ag; Fig. S4A–D, ESI<sup>†</sup>), which results from the robust assembly between two icosahedral subunits. The Ag(icosahedral surface)–Cl(waist) bond lengths of  $\text{Au}_{19}\text{Ag}_{12}$  are much longer than those of  $\text{Au}_{13}\text{Ag}_{12}\text{-Cl}$ , and such an elongation originates from the more twisted assembly between two icosahedral  $\text{Au}_7\text{Ag}_6$  subunits in  $\text{Au}_{19}\text{Ag}_{12}$  (Fig. S4E, ESI<sup>†</sup>). The most significant difference in bond length lies in the Ag(icosahedral surface)–S(waist) interactions between  $\text{Au}_{19}\text{Ag}_{12}$  and  $\text{Au}_{13}\text{Ag}_{12}\text{-S}$  nanoclusters, where the average Ag(icosahedral surface)–S(waist) bond length in  $\text{Au}_{19}\text{Ag}_{12}$  is 2.515 Å, much longer than that of  $\text{Au}_{13}\text{Ag}_{12}\text{-S}$  (2.432 Å; Fig. S4F, ESI<sup>†</sup>). Such a difference is rational, given that the S-Adm ligand in  $\text{Au}_{19}\text{Ag}_{12}$  is bulkier than  $\text{SC}_2\text{H}_4\text{Ph}$  in  $\text{Au}_{13}\text{Ag}_{12}\text{-S}$ , resulting in extended metal–thiol interactions in  $\text{Au}_{19}\text{Ag}_{12}$  so that the bulky S-Adm ligands can be installed into the limited space at the cluster waist.

Because of their different molecular configurations and intercluster interactions, these four  $\text{M}_{13}$ -based nanoclusters exhibit disparate crystal packing modes (Fig. S5, ESI<sup>†</sup>). The ligand-directed intercluster packings of these  $\text{M}_{13}$ -based

nanoclusters were then compared. Specifically, both  $\text{Au}_{13}\text{Ag}_{12}\text{-S}$  and  $\text{Au}_{13}\text{Ag}_{12}\text{-Cl}$  nanoclusters contain C–H···π and H···Cl interactions, while there are only C–H···π interactions in the crystal structure of  $\text{Au}_{13}\text{-DPPM}$ . For the  $\text{Au}_{19}\text{Ag}_{12}$  nanocluster, several types of intercluster interactions are detected, including C–H···π, H···Cl, and π···π interactions (Fig. S5, ESI<sup>†</sup>).

The optical absorptions of these icosahedron-based nanoclusters were then compared. The  $\text{CH}_2\text{Cl}_2$  solution of the  $\text{Au}_{19}\text{Ag}_{12}$  nanocluster showed three distinct absorptions at 455, 515, and 710 nm and two shoulder bands at 415 and 535 nm (Fig. S6, ESI<sup>†</sup>). By comparison, the UV-vis spectrum of the  $\text{Au}_{13}\text{Ag}_{12}\text{-S}$  nanocluster displayed three absorptions at 425, 480, and 650 nm, while those of the  $\text{Au}_{13}\text{Ag}_{12}\text{-Cl}$  nanocluster were centered at 420, 510, and 645 nm. The mono-icosahedral  $\text{Au}_{13}\text{-DPPM}$  nanocluster exhibited an intense band at 440 nm and a shoulder band around 800 nm (Fig. S7, ESI<sup>†</sup>). Such differences in optical absorptions of these icosahedron-based nanoclusters originated from their distinct electronic structures. Yuan *et al.* have unveiled the strong electron coupling between substituent icosahedral units based on the mono-icosahedral  $\text{Ag}_{13}$  and tetra-icosahedral  $\text{Ag}_{61}$  nanoclusters, which resulted in the red-shift of their main absorptions.<sup>40</sup> In this work, the red-shifted absorption was also observed by comparing the intense optical bands of bi-icosahedral  $\text{Au}_{19}\text{Ag}_{12}$ ,  $\text{Au}_{13}\text{Ag}_{12}\text{-S}$ , and  $\text{Au}_{13}\text{Ag}_{12}\text{-Cl}$  nanoclusters (710, 650, and 645 nm, respectively) with the main absorption of the mono-icosahedral  $\text{Au}_{13}\text{-DPPM}$  nanocluster (440 nm), which might also arise from the electron coupling between the substituent icosahedral subunits. Of note, for the  $\text{Au}_{13}\text{-DPPM}$

nanocluster, its 440 nm absorption was regarded as the main absorption of the icosahedral kernel since the  $M_{13}$ -based absorptions (or electronic transitions) were always located in nearby areas.<sup>56–58</sup> In addition, owing to the complete protection of the  $Au_{13}Ag_{12}$  biicosahedral kernel by bridging Cl and surface  $Au_1(DPPM)_1(SR)_1$  structures, the  $Au_{19}Ag_{12}$  nanocluster was highly stable and could maintain its composition and configuration within 20 days, derived from its unchanged optical absorptions over time (Fig. S8, ESI†).

The photoluminescent properties of these four nanoclusters were then compared. As shown in Fig. S9, ESI† the mono-icosahedral  $Au_{13}$ -DPPM was non-emissive, while the other three biicosahedral nanoclusters were emissive. Specifically, the PL intensity of these emissive nanoclusters followed a sequence of  $Au_{13}Ag_{12}\cdot S > Au_{13}Ag_{12}\cdot Cl > Au_{19}Ag_{12}$ . As for the emissive wavelength, the  $Au_{19}Ag_{12}$ ,  $Au_{13}Ag_{12}\cdot S$ , and  $Au_{13}Ag_{12}\cdot Cl$  nanoclusters emitted at 825, 735, and 765 nm, respectively. In this context, the emission wavelength of  $Au_{19}Ag_{12}$  occurred in the NIR-I region and exhibited a significant red-shift relative to those of  $Au_{13}Ag_{12}\cdot S$  and  $Au_{13}Ag_{12}\cdot Cl$  (Fig. S9, ESI†).

### 3. Conclusions

In summary, the horizontal expansion of the rod-like biicosahedral  $M_{25}$  cluster framework was accomplished, yielding an  $[Au_{19}Ag_{12}(S-Adm)_6(DPPM)_6Cl_7]^{2+}$  nanocluster. The structural determination resolved two decades-long questions towards rod-shaped multi-icosahedral nanoclusters, including (i) how to install bidentate phosphine ligands onto the nanocluster shoulder and (ii) how to load bulky thiol ligands into the limited space of the nanocluster waist? A combination of the new  $[Au_{19}Ag_{12}(S-Adm)_6(DPPM)_6Cl_7]^{2+}$  nanocluster in this work and previously reported  $[Au_{13}Ag_{12}(PPh_3)_{10}Cl_8]^{2+}$  or  $[Au_{13}Ag_{12}(SR)_5(PPh_3)_{10}Cl_2]^{2+}$  constituted a platform for mapping out the ligand effect in vertically/horizontally expanding icosahedral  $M_{13}$ -based nanoclusters. Overall, this work presents the horizontal expansion of rod-shaped nanoclusters, which broadens the research towards the “cluster of clusters” and hopefully inspires more work on constructing  $M_{13}$ -based aggregates from vertically and horizontally growing extensions.

### Data availability

All the data supporting this article have been included in the main text and the ESI.†

### Author contributions

C. Z. and P. P. carried out the experiments and analyzed the data. X. W., Z. L. and C. C. assisted the analysis. X. K. and M. Z. designed the project, analyzed the data, and wrote the manuscript.

### Conflicts of interest

There are no conflicts to declare.

### Acknowledgements

We acknowledge the financial support provided by the National Natural Science Foundation of China (21631001, 21871001, and 22101001), the Ministry of Education, and the University Synergy Innovation Program of Anhui Province (GXXT-2020-053).

### References

- 1 R. Jin, C. Zeng, M. Zhou and Y. Chen, *Chem. Rev.*, 2016, **116**, 10346–10413.
- 2 I. Chakraborty and T. Pradeep, *Chem. Rev.*, 2017, **117**, 8208–8271.
- 3 X. Kang, Y. Li, M. Zhu and R. Jin, *Chem. Soc. Rev.*, 2020, **49**, 6443–6514.
- 4 S. Sharma, K. Chakrahari, J. Saillard and C. W. Liu, *Acc. Chem. Res.*, 2018, **51**, 2475–2483.
- 5 T. Kawawaki, Y. Kataoka, M. Hirata, Y. Iwamatsu, S. Hossain and Y. Negishi, *Nanoscale Horiz.*, 2021, **6**, 409–448.
- 6 Y. Jin, C. Zhang, X. Dong, S. Zang and T. C. W. Mak, *Chem. Soc. Rev.*, 2021, **50**, 2297–2319.
- 7 J. Yan, B. K. Teo and N. Zheng, *Acc. Chem. Res.*, 2018, **51**, 3084–3093.
- 8 X. Kang and M. Zhu, *Chem. Soc. Rev.*, 2019, **48**, 2422–2457.
- 9 A. W. Cook and T. W. Hayton, *Acc. Chem. Res.*, 2018, **51**, 2456–2464.
- 10 N. Xia and Z. Wu, *Chem. Sci.*, 2021, **12**, 2368–2380.
- 11 S. Kenzler and A. Schnepf, *Chem. Sci.*, 2021, **12**, 3116–3129.
- 12 G. Salassa and T. Bürgi, *Nanoscale Horiz.*, 2018, **3**, 457–463.
- 13 M. Agrachev, M. Ruzzi, A. Venzo and F. Maran, *Acc. Chem. Res.*, 2019, **52**, 44–52.
- 14 K. Kwak and D. Lee, *Acc. Chem. Res.*, 2019, **52**, 12–22.
- 15 B. Nieto-Ortega and T. Bürgi, *Acc. Chem. Res.*, 2018, **51**, 2811–2819.
- 16 M. Hesari, H. Ma and Z. Ding, *Chem. Sci.*, 2021, **12**, 14540–14545.
- 17 X.-Q. Liang, Y.-Z. Li, Z. Wang, S.-S. Zhang, Y.-C. Liu, Z.-Z. Cao, L. Feng, Z.-Y. Gao, Q.-W. Xue, C.-H. Tung and D. Sun, *Nat. Commun.*, 2021, **12**, 4966.
- 18 E. Ubasart, I. M. Marin, J. M. Asensio, G. Mencia, Á. López-Vinasco, C. García-Simón, I. Rosal, R. Poteau, B. Chaudret and X. Ribas, *Nanoscale Horiz.*, 2022, **7**, 607–615.
- 19 S. Li, X.-Y. Dong, K.-S. Qi, S.-Q. Zang and T. C. W. Mak, *J. Am. Chem. Soc.*, 2021, **143**, 20574–20578.
- 20 R. W. Y. Man, H. Yi, S. Malola, S. Takano, T. Tsukuda, H. Häkkinen, M. Nambo and C. M. Crudden, *J. Am. Chem. Soc.*, 2022, **144**, 2056–2061.
- 21 T. Kawawaki, Y. Kataoka, M. Hirata, Y. Akinaga, R. Takahata, K. Wakamatsu, Y. Fujiki, M. Kataoka, S. Kikkawa, A. S. Alotabi, S. Hossain, D. J. Osborn, T. Teranishi,

- G. G. Andersson, G. F. Metha, S. Yamazoe and Y. Negishi, *Angew. Chem., Int. Ed.*, 2021, **60**, 21340–21350.
- 22 Z.-J. Guan, R.-L. He, S.-F. Yuan, J.-J. Li, F. Hu, C.-Y. Liu and Q.-M. Wang, *Angew. Chem., Int. Ed.*, 2022, **61**, e202116965.
- 23 H. Yi, S. M. Han, S. Song, M. Kim, E. Sim and D. Lee, *Angew. Chem., Int. Ed.*, 2021, **60**, 22293–22300.
- 24 G. Deng, B. K. Teo and N. Zheng, *J. Am. Chem. Soc.*, 2021, **143**, 10214–10220.
- 25 G.-T. Xu, X.-Y. Chang, K.-H. Low, L.-L. Wu, Q. Wan, H.-X. Shu, W.-P. To, J.-S. Huang and C.-M. Che, *Angew. Chem., Int. Ed.*, 2022, **61**, e202200748.
- 26 G. Li, X. Sui, X. Cai, W. Hu, X. Liu, M. Chen and Y. Zhu, *Angew. Chem., Int. Ed.*, 2021, **60**, 10573–10576.
- 27 S. Lee, M. S. Bootharaju, G. Deng, S. Malola, H. Häkkinen, N. Zheng and T. Hyeon, *J. Am. Chem. Soc.*, 2021, **143**, 12100–12107.
- 28 X. Kang, X. Wei, S. Jin, Q. Yuan, X. Luan, Y. Pei, S. Wang, M. Zhu and R. Jin, *Proc. Natl. Acad. Sci. U.S.A.*, 2019, **116**, 18834–18840.
- 29 M. Qu, H. Li, L.-H. Xie, S.-T. Yan, J.-R. Li, J.-H. Wang, C.-Y. Wei, Y.-W. Wu and X.-M. Zhang, *J. Am. Chem. Soc.*, 2017, **139**, 12346–12349.
- 30 N. A. Sakthivel and A. Dass, *Acc. Chem. Res.*, 2018, **51**, 1774–1783.
- 31 X. Kang and M. Zhu, *Coord. Chem. Rev.*, 2019, **394**, 1–38.
- 32 B. K. Teo and H. Zhang, *Coord. Chem. Rev.*, 1995, **143**, 611–636.
- 33 B. K. Teo and H. Zhang, *Inorg. Chim. Acta*, 1988, **144**, 173–176.
- 34 B. K. Teo and H. Zhang, *Polyhedron*, 1990, **9**, 1985–1999.
- 35 B. K. Teo and H. Zhang, *J. Cluster Sci.*, 1990, **2**, 223–228.
- 36 Y. Shichibu, Y. Negishi, T. Watanabe, N. K. Chaki, H. Kawaguchi and T. Tsukuda, *J. Phys. Chem. C*, 2007, **111**, 7845–7847.
- 37 M. S. Bootharaju, S. M. Kozlov, Z. Cao, M. Harb, N. Maity, A. Shkurenko, M. R. Parida, M. N. Hedhili, M. Eddaoudi, O. F. Mohammed, O. M. Bakr, L. Cavallo and J. Basset, *J. Am. Chem. Soc.*, 2017, **139**, 1053–1056.
- 38 R. Jin, C. Liu, S. Zhao, A. Das, H. Xing, C. Gayathri, Y. Xing, N. L. Rosi, R. R. Gil and R. Jin, *ACS Nano*, 2015, **9**, 8530–8536.
- 39 T.-H. Chiu, J.-H. Liao, F. Gam, I. Chantrenne, S. Kahlal, J.-Y. Saillard and C. W. Liu, *J. Am. Chem. Soc.*, 2019, **141**, 12957–12961.
- 40 S. Yuan, C. Xu, W. Liu, J. Zhang, J. Li and Q. Wang, *J. Am. Chem. Soc.*, 2021, **143**, 12261–12267.
- 41 S. Yang, J. Chai, T. Chen, B. Rao, Y. Pan, H. Yu and M. Zhu, *Inorg. Chem.*, 2017, **56**, 1771–1774.
- 42 S. Yang, J. Chai, Y. Lv, T. Chen, S. Wang, H. Yu and M. Zhu, *Chem. Commun.*, 2018, **54**, 12077–12080.
- 43 Y. Song, F. Fu, J. Zhang, J. Chai, X. Kang, P. Li, S. Li, H. Zhou and M. Zhu, *Angew. Chem., Int. Ed.*, 2015, **54**, 8430–8434.
- 44 H. Qian, W. T. Eckenhoff, Y. Zhu, T. Pintauer and R. Jin, *J. Am. Chem. Soc.*, 2010, **132**, 8280–8281.
- 45 L. Xu, Q. Li, T. Li, J. Chai, S. Yang and M. Zhu, *Inorg. Chem. Front.*, 2021, **8**, 4820–4827.
- 46 S. Jin, M. Zhou, X. Kang, X. Li, W. Du, X. Wei, S. Chen, S. Wang and M. Zhu, *Angew. Chem., Int. Ed.*, 2020, **59**, 3891–3895.
- 47 F. Hu, Z. Guan, G. Yang, J. Wang, J. Li, S. Yuan, G. Liang and Q. Wang, *J. Am. Chem. Soc.*, 2021, **143**, 17059–17067.
- 48 S. Wang, X. Meng, A. Das, T. Li, Y. Song, T. Cao, X. Zhu, M. Zhu and R. Jin, *Angew. Chem., Int. Ed.*, 2014, **53**, 2376–2380.
- 49 B. K. Teo and H. Zhang, *Angew. Chem., Int. Ed. Engl.*, 1992, **104**, 445–447.
- 50 S. Jin, W. Du, S. Wang, X. Kang, M. Chen, D. Hu, S. Chen, X. Zou, G. Sun and M. Zhu, *Inorg. Chem.*, 2017, **56**, 11151–11159.
- 51 M. Walter, J. Akola, O. Lopez-Acevedo, P. D. Jadzinsky, G. Calero, C. J. Ackerson, R. L. Whetten, H. Grönbeck and H. Häkkinen, *Proc. Natl. Acad. Sci. U.S.A.*, 2008, **105**, 9157–9162.
- 52 A. Desireddy, B. E. Conn, J. Guo, B. Yoon, R. N. Barnett, B. M. Monahan, K. Kirschbaum, W. P. Griffith, R. L. Whetten, U. Landman and T. P. Bigioni, *Nature*, 2013, **501**, 399–402.
- 53 X. Kang, S. Jin, L. Xiong, X. Wei, M. Zhou, C. Qin, Y. Pei, S. Wang and M. Zhu, *Chem. Sci.*, 2020, **11**, 1691–1697.
- 54 X. Kang, F. Xu, X. Wei, S. Wang and M. Zhu, *Sci. Adv.*, 2019, **5**, eaax7863.
- 55 C. Xu, Q. Yuan, X. Wei, H. Li, H. Shen, X. Kang and M. Zhu, *Chem. Sci.*, 2022, **13**, 1382–1389.
- 56 M. Zhu, C. M. Aikens, F. J. Hollander, G. C. Schatz and R. Jin, *J. Am. Chem. Soc.*, 2008, **130**, 5883–5885.
- 57 K. L. D. M. Weerawardene, P. Pandeya, M. Zhou, Y. Chen, R. Jin and C. M. Aikens, *J. Am. Chem. Soc.*, 2009, **141**, 18715–18726.
- 58 J. Kong, W. Zhang, Y. Wu and M. Zhou, *Aggregate*, 2022, DOI: [10.1002/agt.2.207](https://doi.org/10.1002/agt.2.207).